

THE RADIO VARIABILITY OF THE GRAVITATIONAL LENS PMN J1838–3427

JOSHUA N. WINN^{1,2}, JAMES E.J. LOVELL³, HAYLEY BIGNALL⁴, BRYAN M. GAENSLER¹,
 TRACY J. GETTS³, LUCYNA KEDZIORA-CHUDCZER³, ROOPESH OJHA³, JOHN E. REYNOLDS³,
 STEVEN J. TINGAY⁵, TASSO TZIOUMIS³, MARK WIERINGA³

ABSTRACT

We present the results of a radio variability study of the gravitational lens PMN J1838–3427. Our motivation was to determine the Hubble constant by measuring the time delay between variations of the two quasar images. We monitored the system for 4 months (approximately 5 times longer than the expected delay) using the Australia Telescope Compact Array at 9 GHz. Although both images were variable on a time scale of a few days, no correlated intrinsic variability could be identified, and therefore no time delay could be measured. Notably, the fractional variation of the fainter image (8%) was greater than that of the brighter image (4%), whereas lensed images of a point source would have the same fractional variation. This effect can be explained, at least in part, as the refractive scintillation of both images due to the turbulent interstellar medium of the Galaxy.

Subject headings: gravitational lensing—techniques: interferometric—quasars: individual
 (PMN J1838–3427)—scattering—radio continuum: ISM

1. INTRODUCTION

Multiple-image gravitational lenses offer a famous and refreshingly direct method for measuring the Hubble constant (H_0), as first envisioned by Refsdal (1964, 1966). If the background source is variable, then the variations of each image are seen at different times, because of the different proper lengths of the image paths. A model of the gravitational potential predicts the time delays in units of H_0^{-1} . Thus, if the model is accurate, measuring the time delays amounts to measuring the Hubble constant. Currently it is believed that H_0 is known within 10%, thanks mainly to hard-won and high-quality data from the *Hubble Space Telescope* Key Project (Freedman et al. 2001), but it is still desirable to develop independent methods of determining H_0 because of the fundamental importance of this quantity in interpreting cosmological observations.

For the time-delay method to succeed, one must obtain light curves of multiple images that have a sufficient duration, sampling rate, and precision for correlated intrinsic variations to be detected. This has proven to be difficult. Time delays have been measured in only 10 systems, and many of those measurements are subject to large uncertainties (for recent reviews, see Kochanek & Schechter 2003 and Courbin, Saha, & Schechter 2002). In addition, the method is limited by systematic errors in lens models, although at least the nature of the degeneracy between the mass distribution and H_0 is well understood (Gorenstein, Shapiro, & Falco 1988; Kochanek 2002). This means that if progress in measuring H_0 by other means continues to outstrip progress in understanding the mass distributions of galaxies, then the time-delay method can be run in reverse: time delays can be used to study galaxy structure, for an assumed value of H_0 (see, e.g., Kochanek 2003).

In this paper we report the results of a campaign with the Australia Telescope Compact Array (ATCA⁶) to monitor

PMN J1838–3427, a two-image lensed quasar discovered by Winn et al. (2000). The next section summarizes the properties of this object and the design of our campaign, which was similar to the successful effort by Lovell et al. (1998) to measure the time delay of PKS 1830–211. Section 3 presents new radio maps based on data from the Very Large Array (VLA⁷). These observations were used to produce a better model of the radio source structure and thereby improve the analysis of the ATCA data. The ATCA observations are described in § 4, and the data reduction procedure is explained in § 5. Correlated variability was not detected, and no time delay could be measured. In fact, excess variability was measured in the fainter image that cannot easily be explained as intrinsic variations or systematic errors. In § 6 we discuss these possibilities and argue that refractive scintillation is the best explanation. In § 7 we summarize our observations and conclusions.

2. DESIGN OF THE CAMPAIGN

The properties of the target object, PMN J1838–3427, were described in detail by Winn et al. (2000). Here we provide a summary. At centimeter wavelengths, the system has a flat spectrum and a total flux density of about 0.3 Jy. It consists of two images (A and B) of a quasar at a redshift of $z = 2.78$, produced by the lensing effect of a radio-quiet foreground galaxy at $z \approx 0.35$. Both images are very compact, even at milliarc-second resolution. Image B is $1''.0$ south of image A, and has a flux density that is approximately 14 times smaller than the flux density of image A.

This object appeared to offer excellent prospects for time-delay measurement. It is bright, by modern standards, which allows for short observations at each epoch, and for self-calibration of antenna-based errors. The flat radio spectrum and the compactness of the radio components are indicators of radio

¹ Harvard-Smithsonian Center for Astrophysics, 60 Garden St., Cambridge, MA 02138

² National Science Foundation Astronomy & Astrophysics Postdoctoral Fellow

³ Australia Telescope National Facility, CSIRO, P.O. Box 76, Epping, NSW 1710, Australia

⁴ Joint Institution for VLBI in Europe, Post Bus 2, 7990 AA, Dwingeloo, The Netherlands

⁵ Centre for Astrophysics and Supercomputing, Swinburne University of Technology, Mail No. 31, P.O. Box 218, Hawthorn, Victoria 3122, Australia

⁶ The ATCA is part of the Australia Telescope, which is funded by the Commonwealth of Australia for operation as a National Facility managed by CSIRO.

⁷ The VLA is operated by the National Radio Astronomy Observatory, a facility of the National Science Foundation operated under cooperative agreement by Associated Universities, Inc.

variability, and indeed, three VLA and ATCA measurements of the total 8.5 GHz flux density by Winn et al. (2000) ranged from 0.18 to 0.27 Jy. Assuming the galaxy mass distribution to be isothermal ($\rho \propto r^{-2}$), lens models predict a time delay of $15h^{-1}$ days.⁸ This is long enough for a sampling rate of once every few days to be sufficient, and short enough for the delay to be measurable in a single season of a few months.

Given its southerly declination, the target is easily observed over a wide range of hour angles from the ATCA site. Although the ATCA is a linear array, and therefore provides only one-dimensional spatial information in a short observation, all that is needed is for some of the projected baselines to be long enough in the north–south direction to resolve the $1''$ double. At an observing frequency of 9 GHz (the highest frequency that was routinely available at the time of our campaign), the rule of thumb $\lambda/2D < 1''$ leads to the criterion $D > 3.4$ km. All of the ATCA’s standard configurations have at least a few baselines satisfying this criterion (although the more extended configurations are obviously preferable). This prevented the campaign from being interrupted by configuration changes.

Because of the north-south orientation of the double, we did not want to observe the target near transit, when the projected baselines are primarily oriented in the east–west direction. Neither did we want to observe the target close to the horizon, where the projected baselines are foreshortened, and where shadowing, spillover, and gain-elevation effects are greatest. Our simulations showed that a good compromise was to observe the object at an hour angle of about +4.5 hours or –4.5 hours.

These considerations determined our observing strategy. Ideally we would observe at 9 GHz, with a sampling interval of 2 days (about one-tenth of the expected time delay), for an entire observing season of 4 months. Each observation was scheduled as close as possible to the optimal hour angles mentioned above. The 9 GHz receivers produce a root-mean-squared (RMS) noise level of 0.12 mJy beam⁻¹ in a 30 minute observation, which is low enough for the thermal noise to be $<1\%$ of the flux density of image B. The consistency in the flux density scale from epoch to epoch is routinely better than 1%, and can be checked via observations of a secondary flux density calibration source. Our simulations suggested that even in the most compact configurations, the flux densities of B and A would be measurable with 2% accuracy, despite the covariance between the components (as discussed further in § 6.3). Thus, if the quasar underwent intrinsic variations of 5–10% or greater, the time delay could be measured.

3. SUPPORTING VLA OBSERVATIONS

A short observation with a linear array such as the ATCA provides sparse and nearly one-dimensional coverage of the spatial Fourier plane (also known as the visibility plane, or (u, v) -plane). The two-dimensional radio source structure cannot be determined independently from such data. In previous observations, the source appeared to consist entirely of two point sources, but in the course of our analysis, we came to suspect that this model was not accurate enough. Furthermore, measurements with a linear array are particularly susceptible to confusion with neighboring compact radio sources. Although there is no source brighter than 50 mJy within a $20'$ search radius of the 1.4 GHz NRAO VLA Sky Survey (NVSS; Condon

et al. 1998), and the nearest NVSS source is $5'$ away and has a flux density of only 3 mJy, it was possible that a compact inverted-spectrum source could be contaminating our 9 GHz visibilities. For these reasons we arranged for VLA observations (with more complete (u, v) -coverage) in order to search for low-surface-brightness sources and confusing sources that might have been missed in previous observations.

We obtained snapshots with the VLA in three of its four configurations: the A array, on 2002 March 4; the B array, on 2002 August 12; and the C array, on 2003 January 5. In all cases, the total observing bandwidth was 100 MHz per polarization in each of two frequency bands, centered on 8435 MHz and 8485 MHz. A short observation of 3C 286 was used to set the flux density scale. The phase calibration source PMN J1820–2528 was observed before and after each observation of PMN J1838–3427. The data were calibrated using standard procedures in AIPS⁹ and mapped with Difmap (Shepherd 1997).

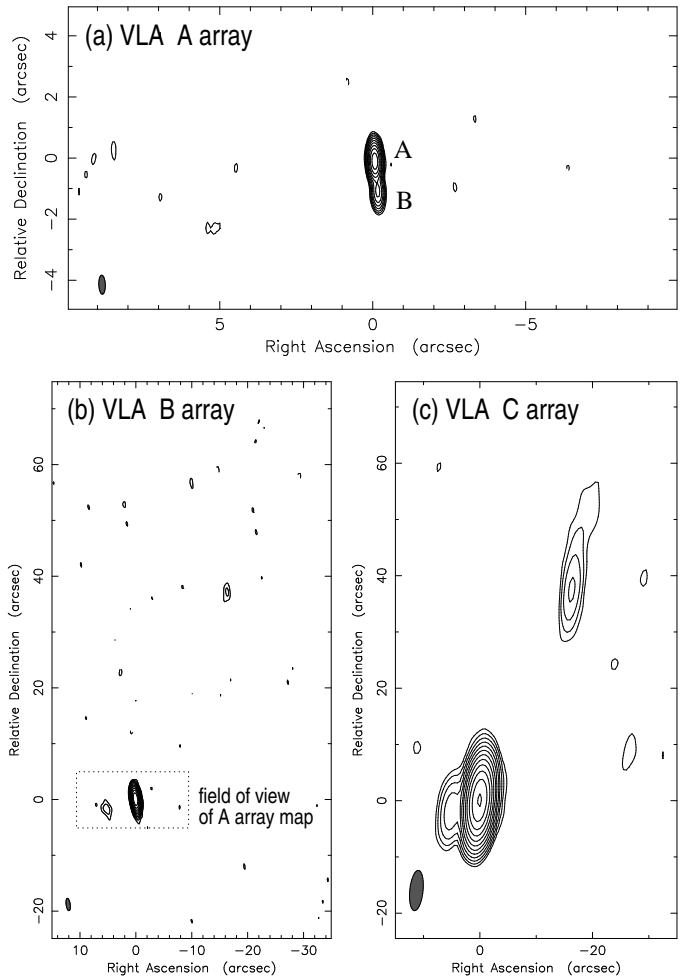


FIG. 1.— 8.5 GHz VLA maps of PMN J1838–3427. All the maps were created using natural weighting of the visibilities. The contour levels are -3σ , 3σ , 6σ , 12σ , etc. The small gray ellipse in the lower left corner illustrates the restoring beam. (a) A array map, with FWHM restoring beam diameters of $0''.62 \times 0''.21$, $\sigma = 0.09$ mJy beam⁻¹. (b) B array map, FWHM $2''.2 \times 0''.7$, $\sigma = 0.08$ mJy beam⁻¹. (c) C array map, FWHM $7''.2 \times 2''.4$, $\sigma = 0.03$ mJy beam⁻¹.

Of the three maps, the A array map (Figure 1a) has the highest angular resolution and the poorest surface-brightness sensi-

⁸ Here, h is defined such that $H_0 = 100h$ km s⁻¹ Mpc⁻¹, and the cosmological model is assumed to be flat, with $\Omega_M = 0.3$ and $\Omega_\Lambda = 0.7$.

⁹ The Astronomical Image Processing System (AIPS) is developed and distributed by the National Radio Astronomy Observatory.

tivity. The quasar images A and B are consistent with point sources. The relative positions of A and B were measured by fitting a 2-point model to the visibility data. The results ($\Delta R.A. = 97$ mas, $\Delta \delta = 991$ mas) are consistent with the more precise results obtained by Winn et al. (2000) with the Very Long Baseline Array (VLBA). The B and C array maps (Figures 1b and 1c) reveal two additional components with lower surface brightness. One of these components is located about $5''$ east of B, and has a total flux density of approximately 1.5 mJy. The other component is located about $40''$ to the northwest, and has a total flux density of approximately 2 mJy. These previously unknown diffuse components are likely to be radio jets associated with the background quasar, although it is also possible that one or both components belong to the foreground object or are unrelated objects. No other radio sources were detected in any of the maps. The widest field of view is available in the C array map, in which there are no confusing sources above 0.3 mJy within a radius of $3'$ (the approximate half-power point of the primary beam).

4. ATCA OBSERVATIONS

The ATCA campaign comprised 54 epochs between 2001 August 31 and 2001 December 31. The average spacing between epochs was 2.4 days. At each epoch, our observing block was at least one hour in duration, although some blocks were longer. The observing bandwidth was 128 MHz per polarization in each of two frequency bands, centered on 8640 MHz and 8896 MHz. Each band was subdivided into 16 channels of width 8 MHz. All linear polarization products were correlated. Typically we observed PMN J1838–3427 for 45 minutes during each session. We also made short observations of three calibration sources: PKS 1934–638, the ATCA primary flux density calibration source; PKS 1718–649, a secondary flux density standard; and PKS 1921–293, a bright and compact radio source. The latter was intended as a gain calibration source, although PKS 1718–649 proved to be better for this purpose, as described below.

The initial calibration was performed with ATCA-specific routines in the MIRIAD software package (Sault, Teuben, & Wright 1995). As a first step, the data were corrected for the elevation-dependence of the antenna gains, using the task ELEVCOR. This task modifies the visibilities using gain curves that were empirically determined by Bignall (2003) for each of the six ATCA antennas. This step is important for any flux density monitoring program, because the gains vary by as much as 4% from the zenith to the lower elevation limit of 12° . It is noteworthy that the gain curve for antenna #6 is quite different from the gain curves of the other antennas. This means that the gain–elevation correction is a function of baseline, rather than being a single multiplicative factor affecting all visibilities. This is of particular significance for our data because antenna #6 forms the longest baselines in the array, and is of crucial importance in resolving the two components of PMN J1838–3427.

After the gain–elevation correction, the data were inspected visually to remove obviously corrupted points and shadowed baselines. The scans on PKS 1934–638 were used to calibrate the delays, band pass, flux density scale, and polarization leakage terms. The scans on PKS 1718–649 were used to determine the antenna gains. Because PKS 1718–649 was observed at nearly the same elevation as PMN J1838–3427, this step acted to eliminate residual gain–elevation effects. (The other calibration source, PKS 1921–293, is closer on the sky to the lens, but

was typically observed at a significantly different elevation angle, and provided poorer correction of gain–elevation effects.) Data from 11 epochs were lost or unusable due to problems such as hardware or software glitches, solar interference, and observer error. The analysis of the data from the useful 43 epochs is presented below.

5. DATA REDUCTION

5.1. Light curve of PKS 1718–649

Gigahertz-peaked spectrum (GPS) sources are often used as interferometric flux density calibration sources because they tend to be compact and flux-stable at radio wavelengths (see, e.g., O’Dea 1998). The radio source PKS 1718–649 is a GPS source and is unresolved by the ATCA at 9 GHz (Tingay et al. 1997). These properties made PKS 1718–649 a potentially useful source for checking the consistency of the flux density scale.

For each epoch in our campaign, a model consisting of a single point source was fitted to the visibility data for PKS 1718–649. The antenna phases were self-calibrated with a 10 s solution interval, and the model-fitting procedure was repeated. The resulting flux density was recorded after three more iterations of self-calibration and model fitting. The two frequency bands were processed separately until this point. The mean of the 8896 MHz time series was 1.4% smaller than the mean of the 8640 MHz time series, as expected from the previously measured radio spectrum of the source (Tingay et al. 1997). We increased the 8896 MHz flux densities by 1.4%, and then averaged the results of the two bands at each epoch. The final light curve is shown in Figure 2a. The error bars span the difference between the results of the two bands (after having normalized the 8896 MHz data). These error bars give an indication of the statistical noise in each measurement. The fluctuations of PKS 1718–649 are small, with an RMS variation of 29 mJy, or 0.7% of the mean flux density of 4.04 Jy.

The local sidereal times of the epochs were strongly clustered around two values, 14:00 and 23:00 (hereafter, “early” and “late”), because of the preference for particular hour angles mentioned in § 2. In Figure 2a, the open symbols represent data from the early LSTs, and the filled symbols represent data from the late LSTs. The different symbol shapes represent different array configurations. The reason for encoding this information in the light curves is that many systematic effects, such as confusion, gain–elevation effects, or errors in the flux density scale, would cause correlations of the measured flux density with either the LST or the array configuration. In this case, there are no significant correlations with either LST or array configuration. (By contrast, when the data were first analyzed without applying any gain–elevation corrections, i.e. omitting ELEVCOR in the procedure described in § 4, there was a strong LST-dependence.)

We conclude that the flux density scale is stable to within 0.7%, and may be even better than that, because some of the variations in PKS 1718–649 could be real variations rather than systematic errors. Subsequent to our campaign, we learned that variability of this source has been observed in other monitoring programs [see, e.g., Gaensler & Hunstead (2000), Kedziora-Chudczer et al. (2001), Tingay et al. (2003), Tingay & de Kool (2003)].

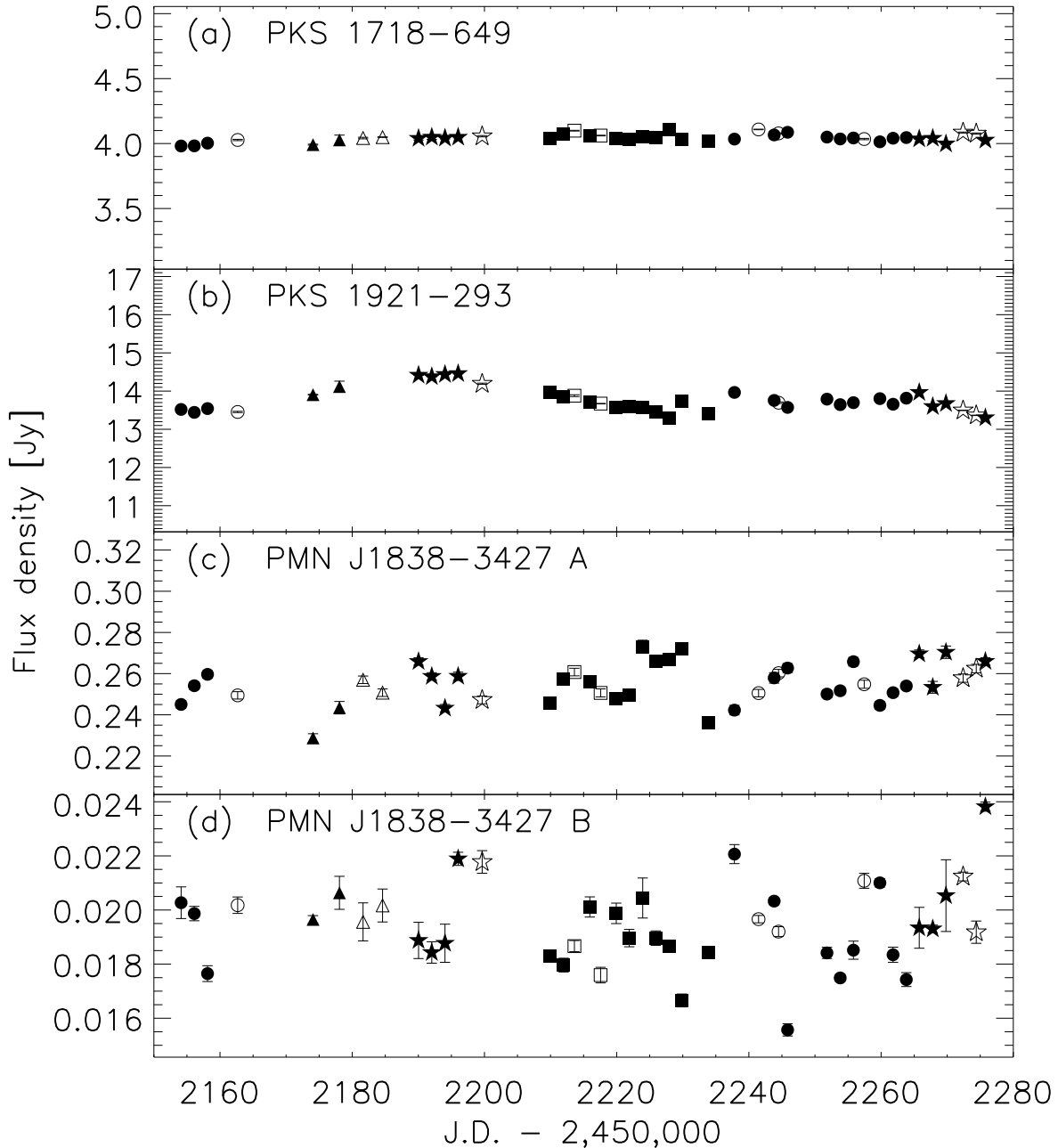


FIG. 2.— ATCA light curves. In each case, the limits of the flux density scale have been set to $\pm 25\%$ of the mean flux density. The symbol shapes encode the ATCA array configuration: circles for 6A, 6B, and 6D; squares for 1.5D; triangles for 0.75D; and stars for EW352. Filled symbols are for measurements at $LST \approx 23$ (“late”) and open symbols are for $LST \approx 14$ (“early”). Where error bars are not seen, they are smaller than the symbol size.

5.2. Light curve of PKS 1921–293

The bright and compact radio source PKS 1921–293 is a blazar that is known to be variable at radio wavelengths (see, e.g., Dent & Balonek 1980; Romero, Benaglia, & Combi 1995; Gaensler & Hunstead 2000). It was observed as a potential gain calibrator, although in the end PKS 1718–649 proved to be more useful for this purpose. Nevertheless we produced a light curve for PKS 1921–293 in exactly the same way as we had for PKS 1718–649. The result is shown in Figure 2b. The RMS variation is 0.3 Jy, or 2.2% of the mean flux density of 13.8 Jy, with a time scale of approximately 20 days from peak to peak. In § 6.4 we consider the possibility that this variation

is due to refractive scintillation, which is relevant to our interpretation of the light curves of PMN J1838–3427.

5.3. Light curves of PMN J1838–3427 A and B

The flux densities of images A and B (S_A and S_B) were measured from the ATCA data using a procedure similar to the one employed for PKS 1718–649 and PKS 1921–293, except that the source model was not a point source. Instead, the model consisted of two point sources with relative positions that were fixed at the values measured in the VLA A array data, and also a model of the two diffuse components discovered in the VLA B array and C array data (§ 3). Ideally, the model should be

based on a sampling of the (u, v) plane that is similar to the sampling of the ATCA monitoring data. The projected baselines of the ATCA data ranged in length from 0 to 140 k λ , with most of the data between 0 and 100 k λ . This matches the range of projected baselines in the B array data better than the A or C array data. Thus, to describe the diffuse components, we used a CLEAN-component representation based upon the B array visibilities with projected baselines shorter than 120 k λ . The positions and flux densities of the CLEAN components were held constant during the fits.

The results from the two frequency bands were processed separately and then averaged, as in § 5.1. The final light curves are plotted in Figure 2c and 2d. The error bars show the quadrature sum of two quantities: the difference between the results of each frequency band (as above), and 0.7% (the uncertainty in the flux density scale). For all the light curves in Figure 2, the limits on the flux density axis were chosen to be $\pm 25\%$ of the mean flux density. This allows for an easy comparison of the fractional variations in each light curve. The hour angle and array configuration of each observation are encoded in the symbols in Figure 2 (see the caption).

The RMS variation of S_A is 9.8 mJy, or 3.8% of the mean flux density of 255 mJy. The time scale of the variations seems to be 5–10 days from peak to peak, with some outliers. The amplitude of the fluctuations is much larger than the statistical error and also larger than the 0.7% variation of PKS 1718–649. We tested for systematic errors by looking for correlations between S_A and the LST, the array configuration, the flux density of PKS 1718–649, and with S_B , but we did not find any significant correlations. For these reasons, it appears that the variations in S_A are not systematic errors but rather are real variations of the radio source. Whether they are intrinsic (due to changes in the quasar luminosity) or extrinsic (due to scintillation) will be taken up in the next section.

The RMS variation of S_B is 1.6 mJy, or 8.0% of the mean flux density of 19.7 mJy. The variations do not appear to be well sampled, implying that the time scale is $\lesssim 2$ days. Again, the amplitude of the fluctuations is larger than the statistical error and the error in the flux density scale, and there are no significant correlations between S_B and the LST, the array configuration, the flux density of PKS 1718–649, or S_A .

6. DISCUSSION

6.1. Absence of correlated intrinsic variability

Lens models generally predict that intrinsic variations of a 2-image quasar should be seen first in the image that is observed further from the center of the lens galaxy. In this case, variations of image A are expected to precede image B; for a model in which the mass distribution of the lens galaxy is isothermal, the delay is $15h^{-1}$ days (Winn et al. 2000). If the observed variability were due entirely to intrinsic variations of the quasar, then one would expect $S_B(t)$ to resemble $S_A(t)$ after scaling it by the magnification ratio and shifting it in time by 15–30 days. Unfortunately, no such correspondence can be discerned in the light curves of Figure 2. There are significant variations in the light curve of image A, as argued in the previous section, but they cannot be matched up to variations in the light curve of image B. Consequently, the time delay could not be measured from these data.

Although apparent to the eye, this fact was confirmed in the following manner. For a given trial value of τ , the A–B time delay, we computed $\sigma(\tau)$, which is defined as the RMS variation

of the “difference light curve”

$$\Delta s(t) = \frac{S_A(t-\tau)}{\langle S_A \rangle} - \frac{S_B(t)}{\langle S_B \rangle}. \quad (1)$$

Here, $\langle S_A \rangle$ and $\langle S_B \rangle$ are the mean values of $S_A(t)$ and $S_B(t)$. The RMS was computed over the time range for which there are overlapping data for $S_A(t-\tau)$ and $S_B(t)$. The interpolation that is necessary for computing $S_A(t-\tau)$ was performed with cubic splines. If the variations in the light curves were purely intrinsic, then $\sigma(\tau)$ would be minimized when τ is the true time delay. The results are shown in Figure 4. There is no clear minimum. The smallest values of σ are obtained for $\tau < 0$, even though we expect $\tau > 0$ because variations of image A should precede variations in image B. We also note there is no significant minimum at $\tau = 0$, confirming our earlier statement that $S_A(t)$ and $S_B(t)$ are not correlated.

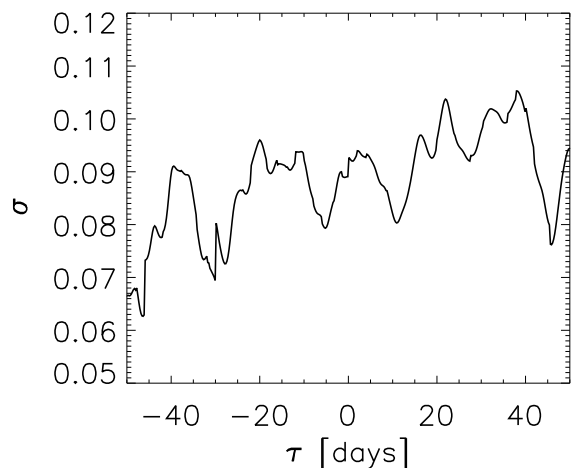


FIG. 3.— The RMS variation of the difference light curve, as a function of the trial value of the time delay. This quantity should be minimized at the true value of the time delay. No clear minimum can be discerned, and therefore no time delay can be measured.

In the rest of this section, we discuss our attempts to understand the reason for the lack of correspondence between the light curves. Apart from the statistical noise (which is negligible for S_A , and small even for S_B), there are three possible sources of variability in the light curves: intrinsic variations of the radio source, unaccounted-for systematic errors in the flux density measurements, and extrinsic variations of the radio source (e.g. scintillation). Below we consider these possibilities in turn.

6.2. Excess variability of image B

It is unlikely that the observed variability in S_B is due entirely (or even mainly) to intrinsic variations of the source—not only because no correlated variability is seen, but also because the fractional variability in S_B is larger than that of S_A . Suppose the quasar is a point source with intrinsic flux density $S(t)$. Then one would expect $S_A(t) = \mu_A S(t-t_0)$ and $S_B(t) = \mu_B S(t-t_0-\tau)$, where μ_A and μ_B are the image magnifications, t_0 is the light-travel time for image A, and τ is the time delay. The fractional variations would be equal, $\frac{\delta S_B}{S_B} = \frac{\delta S_A}{S_A} = \frac{\delta S}{S}$, whereas in reality $\frac{\delta S_B}{S_B} \approx 2 \frac{\delta S_A}{S_A}$. Since the monitoring duration was 5 times longer than the expected time delay, the excess variability in image B is unlikely to be a fluke.

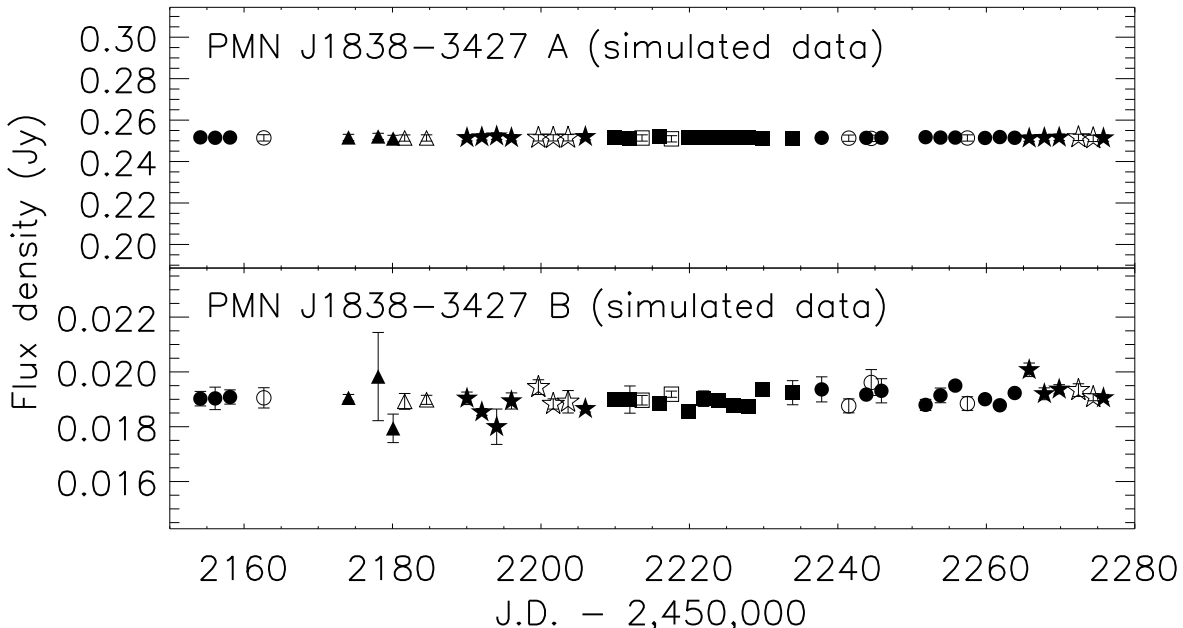


FIG. 4.— ATCA light curves of two images of PMN J1838–3427, based on simulated data with the same receiver noise and (u, v) -coverage as the real data. The symbol conventions are the same as in Figure 2.

One way to escape the conclusion that the variability cannot be intrinsic is to suppose that the variable portion of image A is blended with a non-variable component that is not doubly imaged. For example, image A may have a jet with flux density S_0 that has no counterpart in image B. This would decrease the fractional variability in S_A without affecting the fractional variability in S_B . The problem is that one would need $S_0 \approx 130$ mJy in order to dilute the fractional variability of A by a factor of 2, and although there is evidence for an extended component near image A, it appears to have a smaller flux density. Winn et al. (2000) found the 5 GHz VLBA flux density of image A to be 55 mJy smaller than the VLA flux density measured 4 months previously. If not due to source variability, the discrepancy could be caused by an extended portion of image A that is blended with the compact point source at arcsecond resolution, but that is nearly invisible at milliarcsecond resolution (due to the lack of short baselines). Since an unknown fraction of this extended component is doubly imaged, and since radio jets tend to have steep radio spectra (i.e. the flux density decreases with increasing frequency), the 9 GHz diluting component should have $S_0 < 55$ mJy.

6.3. Simulated data

In previous sections we discussed tests for possible systematic errors due to an inaccurate source model, confusing sources, and residual gain–elevation effects. The excess variability of component B does not seem to be caused by any of these effects. The light curves did not change appreciably when the source model was altered to include the diffuse components discovered with the VLA. No confusing sources were found, and there are no detectable phase slopes in the visibility data that would indicate a confusing source. There are no significant correlations between the flux densities and the elevation angle, or array configuration.

In this section we discuss an additional concern: given that

the longest ATCA baselines were only just sufficient to resolve the double, there is a potentially large covariance between S_A and S_B . For this reason, as mentioned in § 2, we performed simulations prior to the campaign to check the accuracy with which we would be able to separate the flux densities of the components. These simulations suggested we could achieve 2% accuracy in S_B despite the small A–B separation. Here we discuss a more detailed simulation based on the actual noise properties of the data, which confirmed our previous estimate of the achievable accuracy.

The light curves are based on the Stokes I (total intensity) data, but the full polarization information was recorded. Since the fractional circular polarization of PMN J1838–3427 is smaller than 0.25%, the Stokes V visibilities from each epoch were nearly consistent with zero, and they had exactly the same statistical noise level and (u, v) coverage as the I data. This made the V data useful for testing purposes.

To the Stokes V visibilities from each epoch, we added a model visibility function appropriate for PMN J1838–3427, using the MIRIAD task UVMODEL. The relative positions of the 2 point sources in the model were fixed at the values measured with VLBI, and the flux densities were set at 0.252 Jy and 0.019 Jy. We then produced light curves from this artificial data set using the same procedure as we had used on the real data. The resulting light curves are in Figure 3. The flux density of image A is recovered with 0.1% precision. There are fluctuations in S_B due to the noise in the visibilities, the model fitting procedure, and varying (u, v) -coverage, but the RMS fractional variation is only 2%. The 8% variations observed in the actual data must have a different origin.

6.4. Extrinsic variability

Compact radio sources scintillate due to scattering by the ionized interstellar medium (ISM), much as stars twinkle due to scattering by the Earth’s atmosphere (see, e.g., Rickett 1990

or Narayan 1992). Is scintillation a plausible explanation for the lack of correlation between the light curves, and in particular for the excess variability of image B? In this section we ask what type and degree of scintillation one might expect to occur along this line of sight through the Galaxy, and whether the amplitude, bandwidth, and time scale of the observed variations are consistent with those expectations.

Walker (1998, 2001) used the Taylor & Cordes (1993) model of the ionized ISM to give rough expectations for the scattering of extragalactic radio sources. According to this model, for the line of sight to PMN J1838–3427 (Galactic longitude $l_{II} = 0^\circ.4$ and latitude $b_{II} = -12^\circ.5$), the transition frequency between strong (multi-path) and weak scattering is $\nu_0 \approx 30$ GHz, with strong scattering occurring for $\nu < \nu_0$ as in our observations. Strong scattering phenomena can be divided into diffractive scintillation, which refers to the interference pattern produced by the multiple image paths, and refractive scintillation, which refers to the focusing and de-focusing of the entire image ensemble (the “scatter-broadened” image). Diffractive scintillation requires a source with an exceptionally small angular size or an exceptionally nearby scattering screen, and is rarely observed for extragalactic radio sources. Hence for our purposes the relevant phenomenon is probably refractive scintillation.

Refractive scintillation produces an RMS intensity modulation of

$$m = \left(\frac{\nu}{\nu_0} \right)^{17/30} \left(\frac{\theta_R}{\theta_S} \right), \quad (2)$$

where θ_S is the angular size of the source and θ_R is the size of the refractive scattering disk. Using the estimates of Walker (2001) we obtain $\theta_R \approx 15 \mu\text{as}$ for the line of sight to PMN J1838–3427 at 9 GHz. For scintillation to produce the observed 4% modulation of image A, a source size of $\theta_S \approx 0.2$ mas is needed. This is consistent with being unresolved in the 5 GHz VLBA map of Winn et al. (2000), which had an angular resolution of 10.5×1.8 mas. It is also consistent with the theoretical lower limit on angular size due to the well known “inverse Compton catastrophe” (Kellermann & Pauliny-Toth 1969): $\theta_S > (0.6 \text{ mas}) \nu^{-1} \sqrt{S}$, where ν is in GHz and S is in Janskys. In this case, the background radio source has a flux density of $S \approx 0.1$ Jy, corresponding to a minimum angular size of $20 \mu\text{as}$. The angular size of image A is approximately twice the intrinsic source size, due to lensing magnification, giving $\theta_A > 40 \mu\text{as}$. Thus, both the observed upper limit and theoretical lower limit on the angular size of image A are consistent with the scintillation hypothesis. Furthermore, one naturally expects the fractional RMS variation of image B to be a few times larger than that of image A, because the angular size of image B is a few times smaller.¹⁰

Refractive scintillation is by nature a broad band phenomenon ($\Delta\nu \sim \nu$), which is consistent with our observation that the modulations were the same in two frequency bands separated by $\Delta\nu = 0.03\nu$. The time scale of the variations depends upon the transverse speed of the scattering screen. Walker (1998), assuming $v \approx 50 \text{ km s}^{-1}$, found the time scale to be

$$t \approx (1.4 \text{ hr}) \left(\frac{\nu_0}{\nu} \right)^{11/5} \left(\frac{\theta_S}{\theta_R} \right). \quad (3)$$

This gives approximately 10 days for $\theta_S = 0.2$ mas, in agreement with the light curve for image A. The time scale is expected to be a few times shorter for image B, again because the

angular size of image B is smaller than that of image A. This is also consistent with the light curves. The lack of correlation between the light curves is also expected, because the $15 \mu\text{as}$ scattering disk is much smaller than the $1''$ separation between the two images. In short, refractive scintillation is expected for this source at 9 GHz, and it can account for the observed amplitudes and time scales of variability of both components.

Having put forth this hypothesis for the observed variations of PMN J1838–3427, one might wonder whether scintillation should also have been observed for PKS 1921–293 or PKS 1718–649. For the line of sight to PKS 1921–293 ($l_{II} = 9^\circ.3$, $b_{II} = -19^\circ.6$), Walker (2001) estimates $\nu_0 \approx 15$ GHz and $\theta_R \approx 5.2 \mu\text{as}$. The 9 GHz source size is $\lesssim 0.4$ mas, given the VLBA map of Fey, Clegg, & Fomalont (1996), and therefore the modulation index due to scintillation should be $\gtrsim 0.01$ and the time scale of the variations should be $\lesssim 15$ days. These figures are in fair agreement with the observed RMS variations of 2.2% on a time scale of about 20 days. Of course, it is possible that some of the observed variations are intrinsic to the blazar, but at least the scintillation hypothesis does not predict more variation than is observed, and therefore does not contradict our observations.

Likewise, for PKS 1718–649 ($l_{II} = 327^\circ.0$, $b_{II} = -15^\circ.8$), Walker (2001) estimates $\nu_0 \approx 15$ GHz and $\theta_R \approx 4.6 \mu\text{as}$. Tingay et al. (2002) showed that the source consists of two components, each about 1 mas in diameter, separated by about 7 mas. Each component should scintillate with RMS variations of approximately 0.3% on a time scale of ≈ 40 days, which is consistent with our observation of little or no fluctuations in flux density.

Finally, we note that Koopmans & de Bruyn (2000) have argued that there is another potential source of extrinsic variability: microlensing due to compact masses in the lens galaxy. It is generally thought that the angular sizes of radio sources are too large to be significantly affected by microlensing by stellar-mass objects. In contrast, Koopmans & de Bruyn (2000) argue that relativistic beaming can allow for radio microlensing by shrinking the effective source size, and that this has been observed in the 2-image lens B1600+434. The basis for their argument that the observed variability is due to microlensing, rather than scintillation, is the frequency dependence of the RMS modulation. Since that information is not available in this case, and since the more conventional explanation of scintillation appears entirely plausible, we do not discuss microlensing further.

7. CONCLUSIONS

In an effort to measure the time delay of the two-image gravitational lens PMN J1838–3427, we monitored the system at 9 GHz for 4 months with the ATCA. We achieved a stability in the flux density scale of 0.7% or better. The brighter quasar image varied at the 4% level, and the fainter quasar image varied at the 8% level. It appears likely that scintillation by the ionized ISM caused the observed variability. The time delay could not be measured from these data because no intrinsic correlated variations could be identified. Although this campaign was not successful in this regard, it is our hope that the description of our campaign, data analysis, and interpretation will be of use in future interferometric monitoring campaigns.

¹⁰ A caveat is that the line of sight to image B passes much closer to the center of the lens galaxy than that of image A. This raises the possibility that the angular size of image B may be larger than expected due to scatter-broadening by the ISM of the lens galaxy, as has been observed in PKS 1830–211 by Jones et al. (1996) and in PMN J0134–0931 by Winn et al. (2003).

The scintillation hypothesis can be tested further with multi-frequency monitoring, by comparing the frequency dependence of the observed variability with the expectations of scattering theory (with the caveat that the scattering medium may not be as simple as the idealized Kolmogorov medium that is assumed in such calculations). Future 9 GHz VLBI maps of PMN J1838–3427 may resolve image A at the ~ 0.2 mas level. Longer term monitoring might reveal the annual variations in time scale that are sometimes observed in scintillating sources (for a recent example, see Bignall et al. 2003). Apart from merely explaining the variability of PMN J1838–3427 observed in our campaign, the observation of two such closely spaced scintillating components may be of intrinsic interest. The time scales and amplitudes of the variations will depend upon the relative dimensions of the two images along the direction of motion of the scattering

screen. These inferred dimensions could be compared with the gravitational lensing model to estimate the direction of motion of the scattering screen. Unknowns such as the intrinsic source morphology, the degree of anisotropic scattering, and possible broadening of the images due to scattering in the lens galaxy, would confuse the issue. Perhaps if one could identify a scintillating four-image lens, the greater number of constraints would allow one to disentangle some of these effects.

We are grateful to Ramesh Narayan for helpful discussions regarding scintillation, Vince McIntyre and Robin Wark for assistance with the ATCA observations, and Barry Clark for allocating *ad hoc* VLA time for supporting observations. This work was supported by the National Science Foundation under Grant No. 0104347.

REFERENCES

- Bignall, H. E. 2003, Ph.D. thesis, Adelaide University
 Bignall, H. E., et al. 2003, *ApJ*, 585, 653
 Condon, J. J., Cotton, W. D., Greisen, E. W., Yin, Q. F., Perley, R. A., Taylor, G. B., & Broderick, J. J. 1998, *AJ*, 115, 1693
 Courbin, F., Saha, P., & Schechter, P. L. 2002, *LNP Vol. 608: Gravitational Lensing: An Astrophysical Tool*, 1 [astro-ph/0208043]
 Dent, W. A. & Balonek, T. J. 1980, *Nature*, 283, 747
 Fey, A. L., Clegg, A. W., & Fomalont, E. B. 1996, *ApJS*, 105, 299
 Freedman, W. L., et al. 2001, *ApJ*, 553, 47
 Gaensler, B. M. & Hunstead, R. W. 2000, *Publications of the Astronomical Society of Australia*, 17, 72
 Gorenstein, M. V., Shapiro, I. I., & Falco, E. E. 1988, *ApJ*, 327, 693
 Jones, D. L., et al. 1996, *ApJ*, 470, L23
 Kedziora-Chudczer, L. L., Jauncey, D. L., Wieringa, M. H., Tzioumis, A. K., & Reynolds, J. E. 2001, *MNRAS*, 325, 1411
 Kellermann, K. & Pauliny-Toth, I. I. K. 1969, *ApJ*, 155, L71
 Kochanek, C. S. 2002, *ApJ*, 578, 25
 Kochanek, C. S. 2003, *ApJ*, 583, 49
 Kochanek, C. S. & Schechter, P. L. 2003, in *Carnegie Observatories Astrophysics Series, Vol. 2: Measuring and Modeling the Universe*, ed. W. L. Freedman (Cambridge: Cambridge Univ. Press), in press [astro-ph/0306040]
 Koopmans, L. V. E. & de Bruyn, A. G. 2000, *A&A*, 358, 793
 Lovell, J. E. J., Jauncey, D. L., Reynolds, J. E., Wieringa, M. H., King, E. A., Tzioumis, A. K., McCulloch, P. M., & Edwards, P. G. 1998, *ApJ*, 508, L51
 Narayan, R. 1992, *Phil. Trans. R. Soc. Lond. A*, 341, 151
 O’Dea, C. P. 1998, *PASP*, 110, 493
 Refsdal, S. 1964, *MNRAS*, 128, 307
 Refsdal, S. 1966, *MNRAS*, 132, 101
 Rickett, B. 1990, *ARA&A*, 28, 561
 Rickett, B. J., Coles, W. A., & Bourgois, G. 1984, *A&A*, 134, 390
 Romero, G. E., Benaglia, P., & Combi, J. A. 1995, *A&A*, 301, 33
 Sault, R. J., Teuben, P. J., & Wright, M. C. H. 1995, *ASP Conf. Ser. 77: Astronomical Data Analysis Software and Systems IV*, 4, 433
 Shepherd, M. C. 1997, *ASP Conf. Ser. 125: Astronomical Data Analysis Software and Systems VI*, 6, 77
 Tingay, S. J., et al. 1997, *AJ*, 113, 2025
 Tingay, S. J., et al. 2002, *ApJS*, 141, 311
 Tingay, S. J. & de Kool, M. 2003, *AJ*, 126, 723
 Tingay, S. J., Jauncey, D. L., King, E. A., Tzioumis, A. K., Lovell, J. E. J., & Edwards, P. G. 2003, *PASJ*, 55, 351
 Walker, M. 1998, *MNRAS*, 294, 307
 Walker, M. 2001, *MNRAS*, 321, 176
 Winn, J. N., et al. 2000, *AJ*, 120, 2868
 Winn, J. N., Kochanek, C. S., Keeton, C. R., & Lovell, J. E. J. 2003, *ApJ*, 590, 26